ELSEVIER

Contents lists available at ScienceDirect

Journal of Materials Science & Technology

journal homepage: www.elsevier.com/locate/jmst



Research Article

In-situ observation of deformation-induced grain reorientation in 718 Ni alloy microlattices



Benjamin Stegman^{a,*}, Phani Saketh Dasika^b, Jack Lopez^a, Anyu Shang^a, Pablo Zavattieri^b, Haiyan Wang^a, Xinghang Zhang^{a,*}

- ^a School of Materials Engineering, Purdue University, West Lafayette IN 47907, USA
- ^b Lyles School of Civil Engineering, Purdue University, West Lafayette IN 47907, USA

ARTICLE INFO

Article history:
Received 14 August 2023
Revised 9 November 2023
Accepted 20 December 2023
Available online 25 February 2024

Keywords: Additive manufacturing Microlattices Tensile deformation Crystal reorientation Finite element modeling

ABSTRACT

Microlattices pose ample opportunity for constructing light weight structures for the automotive and aerospace industries. Laser powder bed fusion is an appealing technique to fabricate these structures because of its capabilities to process high-resolution complex architectured structures. In this work we explore the use of a 718 oxide dispersion strengthened alloy to create three microlattice structures designed in nTop, a straight bar, honeycomb and body-centered cubic (BCC) microlattice and investigate the effects of architectures on tensile behavior of the microlattices in a scanning electron microscope. The straight bar configurations deliver high strength but low ductility. The BCC lattices are highly deformable but soft. The honeycomb has an attractive combination of high strength and pronounced work hardening. Furthermore, electron backscattered diffraction studies revealed substantial crystallographic reorientation and grain refinement in the honeycomb lattice during deformation, in contrast to little crystal orientation change in the straight bar specimens. This study suggests that architectures play a significant role in the tensile behavior and deformation mechanisms in metallic materials.

© 2024 Published by Elsevier Ltd on behalf of The editorial office of Journal of Materials Science &

1. Introduction

Additive manufacturing (AM) techniques have gained large amounts of traction in the past decade as the understanding and confidence in quality control in these processes have improved. One of the most used processes for metallic AM is laser powder bed fusion (LPBF), which employs a focused conical laser to selectively melt regions of a metallic powder bed. LPBF is positioned well for production of geometrically complex parts because of the small layer thickness and small laser interaction volume [1].

One subset of complex geometrical parts that has been fabricated by LPBF is metallic microlattices. These are systems comprised of 2D/3D unit cells that are repeated over a volume that results in continuous, low-density structures. Therefore, these designs are critical to light-weighting systems for the automotive and aviation/space industries where additional weight can be expensive and detrimental [2,3]. Other applications include high strain-rate specific energy absorption, where microlattices have shown significant improvement over their conventional bulk counterparts, mod-

E-mail addresses: bstegma@purdue.edu (B. Stegman), xzhang98@purdue.edu (X. Zhang).

ulus regulation for proper medical prosthetics acceptance to bone via stress shielding and generating a negative Poisson's ratio using so-called "auxetic" structures [4–6]. Other techniques that produce similar structures are investment casting, ink jet writing, variants of stereolithography and aerosol jet printing [7–10]. Each process has various trade-offs, including the ability to process different materials (i.e. polymers or ceramics), geometry and size resolution limitations, which ultimately make LPBF a compelling solution for metallic microlattice production. LPBF provides high-resolution capabilities with a fine laser spot size and does not require any necessary post-processing steps prior to use.

Because of massive design space and high cost of experimental data on real parts, validation of finite element model prediction of the complex mechanical deformation response is necessary to optimize mechanical performance expediently with diminished costs. Many aspects from the overall lattice repeating structure, the strut geometry, node geometry, local microlattice density (gradient lattice design) and the microlattice material are tunable. This customizability and high precision position LPBF at the forefront of producing optimal metallic microlattices [11]. Common repeating structures include cubic, body-centered cubic (BCC), honeycomb, diamond, gyroid and many other variant structures [5]. The struts, which connect repeating units, have many geometri-

^{*} Corresponding authors.

cal factors like length, radius, and curvature, all of which affect the mechanical properties and final deformation behavior [12]. Algardh et al. showed that controlling the thickness of the thin-wall sections can affect the ultimate tensile strength (UTS) by governing the cooling rate during solidification and therefore tailoring the grain size [13]. In addition to grain size, crystallographic orientation also plays a significant role in the mechanical response of these metallic samples, but this aspect is rarely discussed [14–16]. This wide microstructure tunability makes the field of microlattice a highly appealing candidate for further exploration.

Alloy 718 (718) is a Ni-based superalloy that is commonly used in the LPBF community due to its great weldability and low cost [17]. Unlike typical superalloys, 718 primarily relies on γ ", a Ni₃Nb precipitate with body-centered tetragonal structure, as its main strengthening mechanism with additional minor strengthening from the γ ', a Ni₃Al ordered face-centered cubic (FCC) precipitate. Our group has recently explored an oxide-dispersion-strengthened (ODS) 718 alloy that showed improved high-temperature mechanical performance [18]. Like many LPBF metals, our 718 ODS alloy showcases a cellular microstructure. In the as-printed (AP) state, these cells are decorated with dislocations and micron size delta and Laves phase precipitates at the cell junctions. The grain morphology is highly anisotropic, with the build direction (BD) displaying elongated grains vs. more equiaxed grains confined in the transverse direction. Nanoscale oxide precipitates formed in the ODS alloy led to improved high temperature strength and ductility comparing with the control 718 alloy without oxide nanoprecipitates [18].

ODS alloys are well-known for their irradiation damage resistance and increasing high-temperature mechanical strength/creep properties [19-21]. Generally, these improved properties derive from a uniform dispersion of oxide nanoparticles with an average diameter in the 10 s of nanometers [22,23]. Not only do these nanoscale dispersoids act as thermally stable dislocation barriers, but they also perform as interface stabilizers, therefore retarding grain growth and recrystallization [24]. These beneficial properties are significant, especially to the aerospace community. Hence, we examine the combination of microlattice designs with an ODS 718 alloy. The hurdles that entail with microlattice production and the deformation mechanisms in an experimental ODS alloy will be illuminated. Analysis of the in-situ mechanical testing results combined with post-deformation microscopy studies showcases new findings on the differences in deformation mechanisms for various microlattice designs.

2. Material and methods

2.1. Experimental methods

nTopology software was leveraged to create multiple microlattice designs (Fig. 1(a)). Three designs, a thin-wall connection tensile lattice (straight bar), a 2D custom-designed honeycomb lattice (honeycomb) and a 2 mm unit cell length BCC microlattice were chosen to be further tested. Each was designed with a 600 µm strut diameter and each with a relative density of 50 %, 48.6 % and 38.2 %. The honeycomb lattice was elongated in the tensile axis to tailor the bending-stretching behavior during deformation. Each design was fabricated via LPBF with an experimental 718 ODS powder on a 316 L stainless steel build plate, by using an SLM 125 LPBF instrument. Our previous work identified that using a laser power of 285 W, 960 mm/s, 110 µm hatch spacing and a 40 µm layer thickness produced the highest density component [18]. A spot size, build plate temperature and oxygen concentration of 70 μm , 80 °C and 0.1 % (1000 ppm) were used, respectively. While our previous work has been cited using the same parameters, it is wise to note that it used an EOS M 290 with a larger spot size that leads to some crystallographic orientation differences. A wire electrical discharge machine (EDM) was used to remove each part from the build-plate. The lattices with 2D symmetry, the straight bar and honeycomb microlattice, were further sectioned via EDM to create ~ 1 mm thick slices for multiple iterations of testing and then polished to a 2000 grit standard using SiC polishing pads.

Scanning electron microscopy (SEM) micrographs were collected on a Thermo Fisher Quanta Field Emission Gun (FEG) 650 scanning electron microscope. Backscattered SEM and energy dispersive spectroscopy (EDS) experiments were performed on a Quanta 650 SEM microscope equipped with an Ametek Hikari detector. An Ametek EDAX Hikari electron backscattering diffraction (EBSD) detector was utilized to quantify grain orientation, grain boundary characteristics and grain size distribution, using a step size of 1 μm . For these SEM experiments, samples were polished to a 2000 grit standard and then polished with a 6-, 3- and 1micron diamond paste polishing media and finished with a submicron colloidal silica step. All tension tests were carried out on a Kammrath-Weiss in-situ tensile frame, inside a Thermo Fischer TeneoVolumescope, using a 10 kN load cell and a constant strain rate of 1 \times 10⁻³ s⁻¹. *In-situ* SEM videos were collected at 5 frames/s at a working distance of 30-40 mm and can be accessed via the Supplementary Information.

2.2. Computational methods

The behavior of all proposed microlattices was simulated under tensile loading using the commercial FE software Abaqus/CAE (version 2021; Dassault Systèmes Simulia Corp., Johnston, RI, USA). One model of each design was created based on the as-fabricated dimensions, which is modified to take into account the defects in 3D printing by measuring average geometrical dimensions of the fabricated model during the early stage of *in-situ* tensile testing.

The straight bar and elongated honeycomb lattices were meshed with 8-node linear brick, reduced integration (C3D8R) elements, while the BCC lattice was meshed with 4-node linear tetrahedron (C3D4) elements. These solid element types were chosen after the finite element discretization was examined for accuracy of solution versus computational expense. Following a convergence study, a maximum permissible mesh size of 0.1 mm across the gauge length was selected. The material properties were calculated by taking the average of the stress-strain data acquired from uniaxial tensile testing of dogbone samples 3D printed with 718 ODS powder, which can be found in Fig. S1 in the supplementary information. To document the evolution of failure in the microlattices during tensile testing, the ductile damage material modeling parameter was adopted. The dogbone of each microlattice had two shoulders, one of which was constrained at all six degrees of freedom, while the other shoulder was coupled to a reference point and allowed to translate freely along the tensile loading axis. At this reference point, displacement-controlled loading along the tensile axis was applied using a dynamic explicit analysis step to mimic the experiments.

3. Results

Fig. 1(a) shows the 718 ODS samples still attached to the 316 L build plate after AM. The three types of specimens tested in this study are shown in optical micrograph in Fig. 1(b). The straight bar samples have a simple, well-defined geometry, making it easier to accurately estimate the stress values by measuring the force values and the cross-sectional thickness from the *in-situ* experiments. The actual wall thicknesses achieved for the straight bar, honeycomb and BCC microlattice specimens are 292 ± 71 , 254 ± 41 and $270 \pm 43~\mu\text{m}$, respectively. Fig. 1(c) shows characteristic stress-strain curves for the three microlattice designs. The BCC lattice has

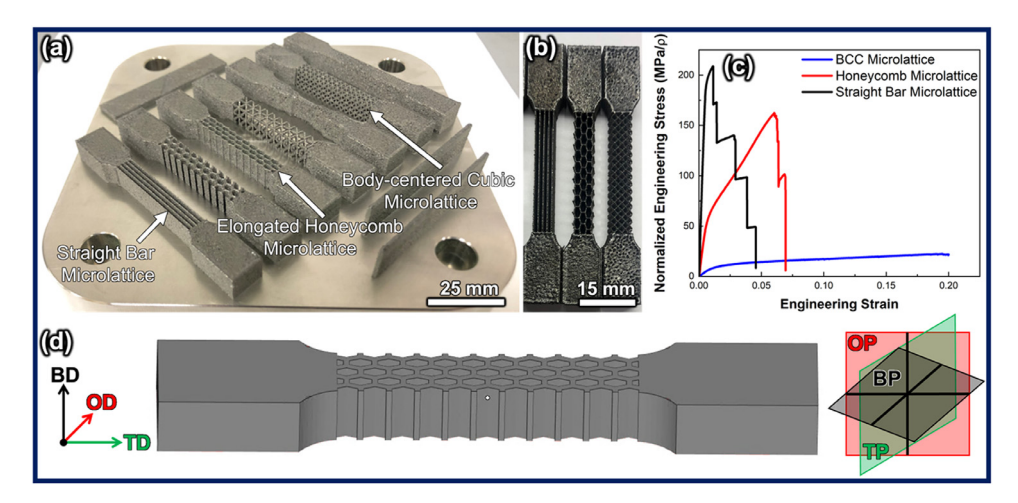


Fig. 1. (a) Optical micrograph of LPBF 718 ODS microlattices, attached to a 316L build plate. (b) Top-down optical image of lattices of interest, including straight bar, elongated honeycomb, and the body-centered cubic (BCC) microlattice (from left to right). (c) Characteristic normalized stress–strain curves of the three types of microlattices. (d) Orientation explanation for directions & planes showing the tensile direction (TD), build direction (BD) and orthogonal direction (OD), and the respective tensile plane (TP), build plane (BP) and orthogonal plane (OP).

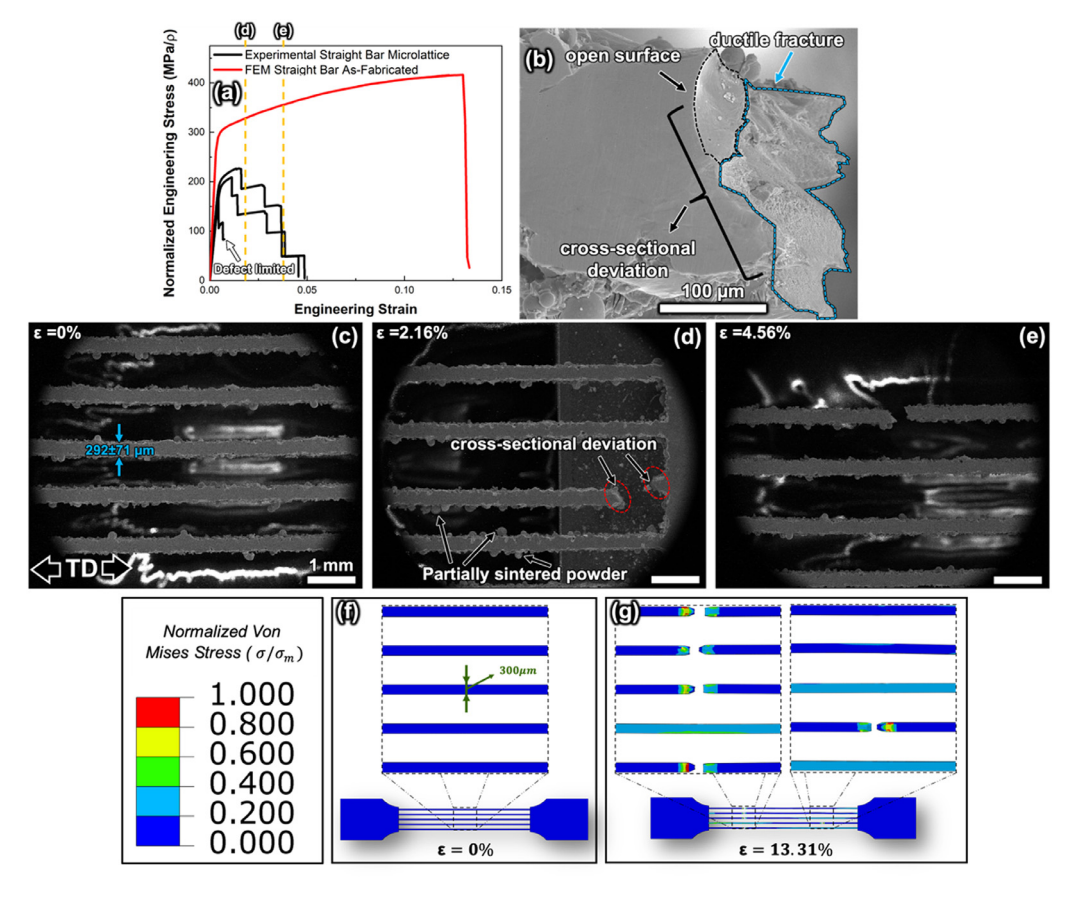


Fig. 2. (a) Normalized engineering stress–strain plots for straight-bar microlattices showing multiple load drops as lattice arms fracture sequentially until final fracture. FEM simulated straight bar microlattice stress–strain curve on the same plot exemplifies the ideal material response. (b) Post-fracture micrograph of fracture surface and defects. (c–e) SEM micrographs captured from *in-situ* mechanical testing at various strains, 0 %, 2.16 % and 4.56 %. (f, g) FEM simulation snapshots of straight bar microlattice at 0 % and 13.31 % strains correspond with the start and completion of the *in-situ* experiments. The color legend denotes the normalized von Mises stresses in the localized areas of each simulation. See supplementary videos 1 and 2 for experimental and simulation details.

the lowest normalized flow stress but sustains large plastic strain (at least 20 %) without fracture. The straight bar specimens have high engineering flow stress but low tensile ductility. The honeycomb microlattice has the flow stress in between the BCC lattice and straight bar specimens and significant work hardening.

The stress-strain curves for the straight bar specimens are compared to the finite element model (FEM) modeling plot in Fig. 2(a).

The work-hardening trends are in general agreement. The morphology evolution of straight bars is shown in SEM micrographs in Fig. 2(c-e). Fracture was observed at numerous beams in the specimens. Premature failure was observed in the straight bar ODS alloy as shown by open surfaces in post-fracture SEM image in Fig. 2(b).

The stress-strain curves for the Honeycomb microlattices (Fig. 3(a)) were normalized by relative density. Different from the

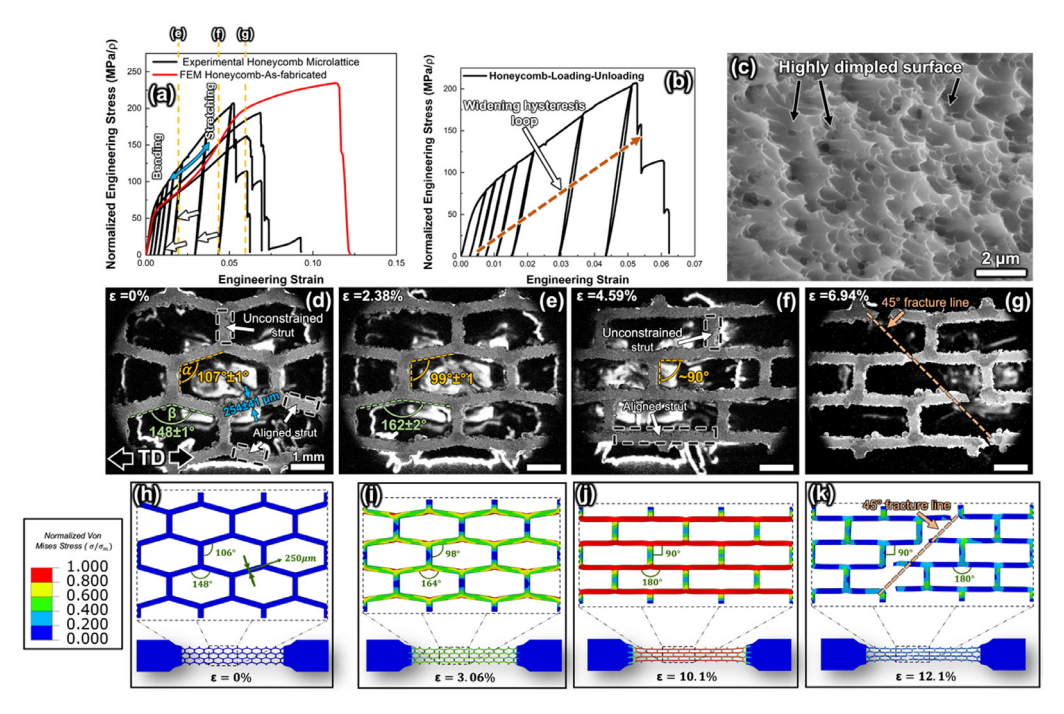


Fig. 3. (a) Normalized stress–strain curves for honeycomb microlattices and the FEM simulated plot demonstrating the concave-up inflection. (b) Loading-unloading experimental stress–strain curve with broadening hysteresis loop as most deformation accumulates. (c) SEM micrograph of fracture surface showing oxide agglomeration and submicron scale ductile dimples. (d–g) *In-situ* SEM micrographs obtained at 0 %, 2.38 %, 4.59 % and 6.94 % strains demonstrating the transition of microlattice from bending to the alignment of the primary arms with the tensile direction, and then to a stretching dominant deformation mechanism. The loading-unloading experiment showed a widening of the hysteresis loop with increasing strain. (h–k) FEM simulation snapshots of the elongated honeycomb microlattice at 0 %, 3.06 %, 10.1 % and 12.1 % strains where the similar evolution of strut angles was observed in comparison to the *in-situ* experiments. The color legend denotes the normalized von Mises stresses in the localized areas of each simulation. See supplementary videos 3 and 4 for experimental and simulation details.

straight-bar specimens, the honeycomb displays a concave-up nature on the stress–strain curves as the test proceeds. *In-situ* SEM micrographs in Fig. 3(d–g) show the internal angle α near the side node of the hexagon (marked by yellow dash lines) evolves from 107° to 99° and 90°, and β near the top-bottom node increases from 148° to 162° and 180°. The loading-unloading plots in Fig. 3(b) showed a widening of the hysteresis loop as the engineering strain increases. FEM analysis in Fig. 3(h–k) revealed initial load localized on the inward joints connecting each unconstrained strut of each hexagon until the load became homogenous throughout the aligned struts.

The BCC microlattice demonstrated the highest deformability to an engineering strain of 20 % without catastrophic failure (Fig. 4(a)). Minor load drops were observed and confirmed to be nodes fracturing. The outstanding tensile ductility of BCC microlattice can be further visualized in Fig. 4(c), which shows severe necking in the post-deformation samples. SEM micrographs in Fig. 4(d-f) captured during the in-situ tests show the internal angle of the nodes decreased from 90° to 71° at the strain of 6.5 %, and then to 57° at the strain of 17.8 %. For the nodes in line with the tensile direction (TD), the angle evolved from 90° to 105° and 121°. The premature fracture illuminates clear load concentrations at the nodes, which are perpendicular to the TD. The FEM simulations show clear load concentrations at the nodes in Fig. 4(g-j) until the final fracture. All in-situ videos for the deformation of these three microlattices can be found in the Supplementary Information.

Challenging EBSD experiments for the deformed microlattices were performed to investigate and visualize differences in grain orientation after tensile deformation. A $\langle 100 \rangle$ out-of-plane texture was observed in inverse pole figures (IPFs) in Fig. 5(c, d) in the gripper section and the node (thin-wall section) of the AP honeycomb lattice. Multiple EBSD scans from other samples have confirmed this preferred out-of-plane crystallographic orientation

and validated via XRD experiments, as seen in Figs. S2 and S3. Post-deformation IPFs in Fig. 6(b) of the straight bar lattice reveal that the tensile stretching deformation to 4 % strain did not cause crystallographic reorientation. Kernel average misorientation (KAM) map in Fig. 6(c) shows that deformation accumulates in the strut locations that are continuous along the TD.

The IPFs for honeycomb microlattice show substantial crystallographic reorientation at 4 % strain (Fig. 6(e)), and maintain a similar crystallographic reorientation until near fracture at 8 % strain (Fig. 6(g)). Fig. S4 demonstrates that this crystallographic rotation occurs in nearly all parts of the honeycomb microlattice, near and further from the fracture surface. This observation was further confirmed in the 3 major axes, BD, TD and orthogonal direction (OD), which lie perpendicular to the TD-OD, BD-OD and BD-TD planes, respectively, in the pole figure analysis completed in Fig 7. KAM maps also exposed that the unconstrained boundary struts (connecting the primary struts) have a substantially lower deformation build-up than the primary struts aligned in the TD at the 4 % strain. The dislocation density in the two types of struts is comparable at the 8 % strain. These key microstructural evolution differences among three types of microlattices lead to different deformation mechanisms upon tensile deformation.

4. Discussion

4.1. Comparison of deformation modes in three microlattices

The three microlattice designs, though comprised of the same 718 ODS alloy, exhibit significantly different mechanical properties due to intrinsic differences brought upon by the specific geometrical designs, as well as the LPBF process. To the best of the authors' knowledge, this is one of the first studies that show manufacturing and mechanical performance of an ODS microlattice

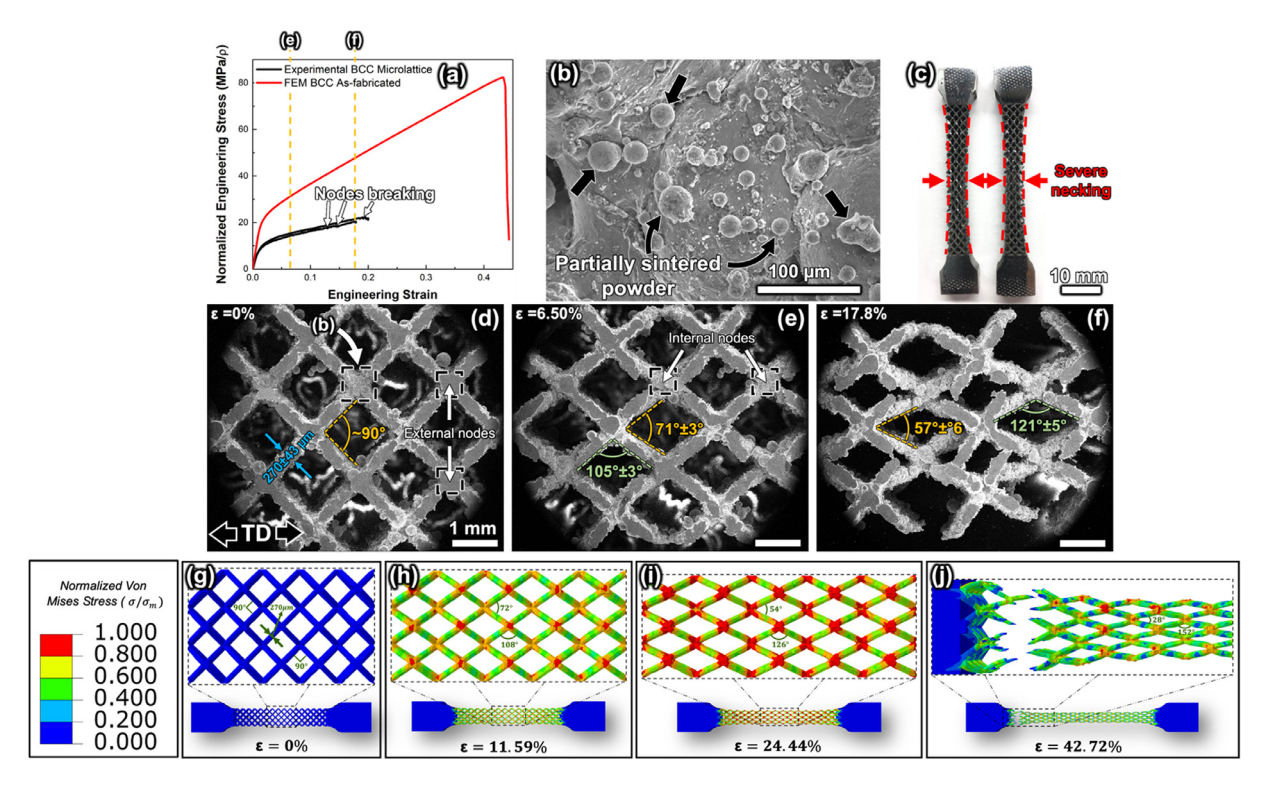


Fig. 4. (a) Normalized stress-strain curves and superimposed FEM simulation for BCC microlattice demonstrating high deformability. (b) *In-situ* micrograph of sample skin decorated with unmelted 718 particles. (c) Optical image showing necking near the center region of each BCC sample. (d–f) *In-situ* SEM micrographs at 0 %, 6.50 % and 17.8 % strains showing angle change of cells. (g–j) FEM simulation snapshots of the BCC microlattice at 0 %, 11.59 %, 24.44 % and 42.72 % strains where a similar evolution of strut angles was observed in comparison to the *in-situ* experiments. The simulations also shows the evolution of stress concentration around the nodes as deformation continues. The color legend denotes the normalized von Mises stresses in the localized areas of each simulation. See supplementary videos 5 and 6 for experimental and simulation details.

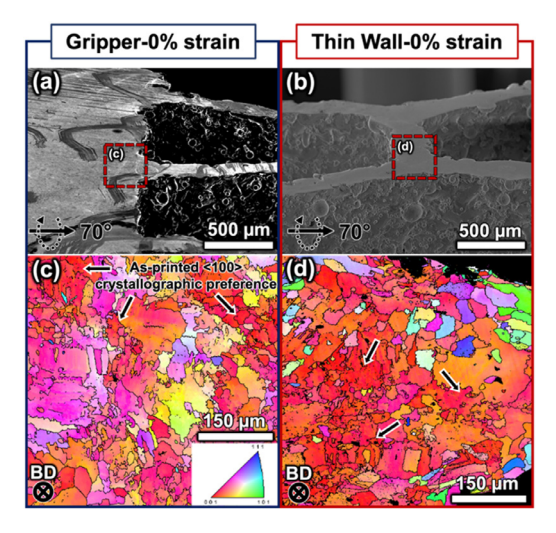


Fig. 5. (a, b) 70° tilted SEM micrographs of the gripper section and thin wall of the honeycomb microlattice. (c, d) The corresponding EBSD inverse pole figure (IPF) maps showing a dominant $\langle 100 \rangle$ crystallographic orientation.

produced via LPBF. The specific parameter sets used in the LPBF process led to all microlattices achieving nearly 50 % of the intended strut diameter of 600 µm, from the stl input file. Weidmann et al. found that depending on the specific parameter sets, the intended thickness of the thin-wall structures could vary by 100 % compared to the minimum achieved in their AlSi10Mg alloy [25]. This variation demonstrates the importance of future parameter exploration for experimental alloy systems like the current 718 ODS alloy. The variability was initially found in the thin-

wall sections of the straight bar lattices that also demonstrated a large variability of cross-section area, with internal porosity extending to the exterior surface. These geometrical defects lead to a reduction in local cross-sectional area and therefore act as stress concentration points. These defects lead to the difference between the simulation and experimental results. The simulations, which assumed a defect-free condition, show specimens deformed in a cup-and-cone manner, typical of a highly deformable material, while the experimental tests generally led to a shear plane, likely due to onset of fracture at defect site due to the stress concentration, although local ductile dimples were observed, as seen in Fig. 3(b, c) [26]. Stress drops occurred due to the sequential fracture of tensile beams in the straight-bar specimens. The tensile results of the straight bars mimic what is achievable from a typical tensile dogbone sample and are used as a reference in this study.

Interestingly, the BCC microlattice with a 3-dimensional design, work hardens in a similar way as the straight bar microlattices, but does contain minor load-drops that correspond with node fractures within the in-situ videos. These load-drops are caused by a combination of the external node damage due to polishing (Fig. 4(e, f)), leading to a reduced thickness, and internal nodes/struts that contained internal defects. Despite the plethora of nodes and large spatial separation, the influence of these defects had a negligible impact on the overall stress-strain curves, as this design reached the highest displacement. The simulations also exhibit that the majority of the stress is distributed around the connecting nodes, putting an excessive sensitivity for each node towards defects, while also decreasing the overall likelihood of premature failure. This stress concentration is generated due to bending of all four connecting struts around the node, compiling the stresses together. Prior FEM simulations have shown similar observations [27–31].

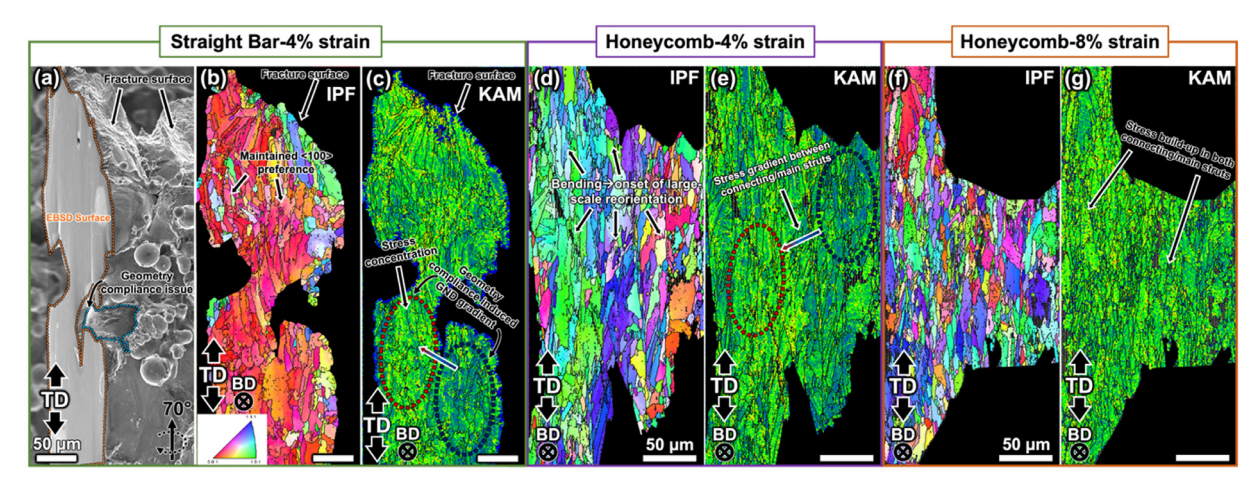


Fig. 6. (a) 70° tilted SEM micrograph of the deformed straight-bar microlattice. (b, c) Respective IPFs and Kernel average misorientation (KAM) maps for the straight-bar strained to 4 %. (d, e) IPF and KAM maps of honeycomb strained to 4 % and (f, g) 8 % strain, highlighting the severe crystallographic re-orientation due to bending deformation.

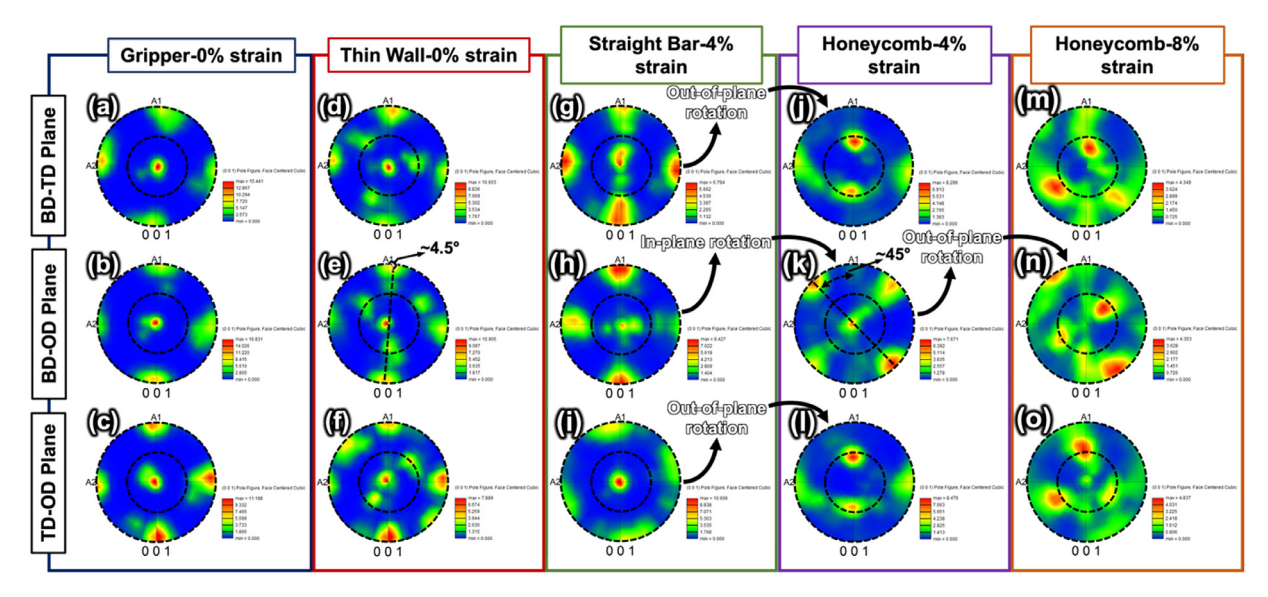


Fig. 7. (a–c) EBSD pole figure analysis along the orthogonal direction (OD), tensile direction (TD) and build direction (BD) of the undeformed honeycomb lattice gripper section (similar to the gripper section in all specimens) showing a primarily $\langle 100 \rangle$ texture. (d–f) EBSD pole figure of the undeformed honeycomb thin wall section showing a primarily $\langle 100 \rangle$ texture in all directions. (g–i) After 4 % strain, the straight bar retained the primary $\langle 100 \rangle$ texture with slight rotation in the build direction. (j–l) After a tension strain of 4 %, the honeycomb lattice showed out-of-plane axis rotations in the build and transverse direction, and in-plane rotation along the tensile direction. (m–o) At 8 % strain, the honeycomb exhibited further out-of-plane rotations in all directions. All pole figures were taken along the [001] zone axis.

Lastly, the honeycomb microlattice deforms in a two-stage deformation mechanism that begins with bending of the top and bottom nodes moving towards the centerline of the sample and then stretching the newly aligned struts. This two-step process creates a unique stress-strain response that results in a concave-up curve (Fig. 3(a)). The inflection point comes when the stretching deformation overtakes the bending as the dominant deformation mechanism. The hysteresis loop widening, as seen in Fig. 3(b) appears similar to the strengthening phenomena reported as back stress [32]. However, this phenomenon could also be caused by the configurational changes of the honeycomb geometry. Interestingly, the FEM simulations also reveal that the unconstrained boundary struts experience lower stresses, in comparison to the aligned struts, supporting the KAM map observation from Fig. 6(e), which shows less deformation accumulation in the unconstrained boundary struts at 4 % strain. The FEM fracture scene also captures the same 45° fracture line between each aligned strut as seen experimentally in Fig. 3(g). A similar feature in the 2D microlattice has been seen in the auxetic structure by Delcuse et al. [33]. These results emphasize the importance of geometric design in changing the deformation behavior of materials.

The straight bar, BCC and honeycomb microlattices exemplify a diverse range of designs that underpin the concept of tailoring deformation behavior by varying extrinsic geometric constraints, which ultimately vary the degree of homogenous/inhomogeneous deformation. Designs that incorporate a majority of bending mechanisms rely heavily on the plastic zone that forms around each node, making the deformation unconstrained, which EBSD highlights as a combination of homogenous and inhomogeneous deformation (KAM-IPF). This stress concentration allows the other regions to minimize their stress state, as shown via digital image correlation and simulations [29-31,34]. This mechanism enhances the damage tolerance of the microlattice, enabling higher levels of ductility. Whereas, designs that partially or fully rely on the stretching deformation, which is induced by a constrained stress state, like the straight bar microlattice, have limited tensile deformability and rely on a homogenous deformation mechanism. The honeycomb, also a 2D design, pushes this limit with the integrated vertical hexagonal nodes that require a shift in the design under initial loads until it reaches its final state with aligned struts. While the BCC and honeycomb microlattices experienced similar inter-strut initial-final angle changes of 32° and 33°, the BCC microlattice has a 3D design, increasing the degrees of freedom and therefore enabling even greater deformability than the honeycomb lattices.

While the main application of these microlattices is in a compressive state, some studies, including our work, focus on uniaxial tension. Nelson et al. revealed that bending-based designs, like the gyroid and octet structures, maintain a high level of deformability in both tension and compression [35]. Each design can be fully optimized for a given stress state via topological optimization, making the concepts very complex [36-39]. Hanzl et al. [40] showcased the idea that stretch-dominated structures maintain superior strength-to-weight ratios, while bending-dominated structures maximize the total energy absorbed, supporting the enhanced ductility argument. Their finding also matches well with the currently observed volume fractions of the microlattice experiencing this unconstrained strain accumulation, which delays ultimate fracture, while also increasing the overall energy absorption with deformation accumulation at the nodes. Understanding these differences between the deformation mechanisms will aid in design optimization and application in various end-use scenarios.

4.2. Crystallographic reorientation

Crystallographic reorientation in a microlattice under tension has not been reported to the best of our knowledge. This kind of microstructural evolution has been reported in standard room temperature compression and tension, high-temperature tension and creep and 3-point bending tests [41-51]. The grain rotations may arise from homogeneous and inhomogeneous deformation. The homogeneous deformation-induced crystal rotation can be accommodated by various deformation mechanisms, such as dislocation slip or twinning. Raabe et al. [45] used FEM simulations of singlecrystal Cu micropillar compression tests to demonstrate that compression and bending caused crystallographic reorientation due to slip. Their simulation demonstrates lattice rotation in single crystals is possible. However, Brown et al. [46] discovered high strain rate compression testing promoted twinning that caused grain rotation throughout the polycrystalline beryllium sample. Conversely, Dumas et al. revealed that twinning occurs in martensitic Ti-6Al-4V dual-phase alloy under a tensile deformation, and leads to crystallographic reorientation that promotes its high ductility [52]. Lastly, Shang et al. [43] have shown via in-situ EBSD coupled with uniaxial tension testing that a nanostructured gradient ferritic steel contained large amounts of lattice rotation in the nanolaminate regions, which enabled the enhancement of the overall mechanical properties. These initial works establish the importance of deformation-induced crystallographic orientation change and the importance of differentiating the homogenous (slipping/twinning) and inhomogeneous (shearing) deformation mechanisms and correlating mechanical properties.

This lattice rotation seems exacerbated by high-temperature deformation as Musinski et al. [49] demonstrated in their gammagamma' strengthened low solvus, high refractory alloys. They concluded that the severe crystallographic reorientation began with the accumulation of geometrically necessary dislocations (GNDs), which induced increasing lattice rotation due to the activation of multiple slip systems. This lattice rotation leads to grain fragmentation where localized and higher degrees of GND build-up cause grain reorientation. In the slower strain rate regions, lattice rotation is a large contributor to strain accumulation. Stinville et al. [53] investigated a high-angle grain boundary of a bicrystal of GTD 444, and the high-temperature creep testing revealed large, localized deformation and lattice rotation at the grain boundary and

at the carbide and eutectic interface with the matrix. Even without grain boundaries, Coakley et al. [54] revealed with EBSD that their CMSX-4 single crystal demonstrated lattice rotation from the (100) to the (020) zone axis in the tertiary creep state, possibly due to shearing at the interface, which is less stiff and leads to higher accumulation of strain. This data supports that, whether a sample has grain boundaries or is a single-crystal, creep testing induces lattice rotation as a mechanism to accommodate deformation. High temperature deformation clearly influences grain boundary stability and promotes grain rotation, at both the quasistatic and creep strain rates. The quasistatic experiments disclose that strain accumulation due to GND activity and multiplication raises wide-spread lattice rotation, while creep allows time for crystallographic reorientation via shear-induced lattice rotation and defect accumulation. Both the homogenous and inhomogeneous deformation mechanisms again play an essential role in these specific hightemperature scenarios for crystallographic rotation.

These previous works studied conventional constrained sample configurations. To date, no work on microlattices has investigated lattice rotations of this nature. Dynamic deformation, with tension, bending and shearing occurring simultaneously throughout a sample, would more accurately portray what proceeded in our honeycomb microlattice, and be considered unconstrained strain. The relevant stress state that bears some similarity to the microlattice deformation may exist from 3-point bending tests. Jin et al. [47] conducted 3-point bending test of a strongly-textured Mg alloy and concluded that the inner wall primarily under a compressive load deforms by twinning, which promotes strong texture changes to a randomly oriented grain morphology. This texture change has a secondary effect by relaxing internal stresses, giving the sample higher ductility. Conversely, Xiao et al. [48] showed, via 3-point bending tests, that a rolled NiTi sheet became highly oriented along the (100) direction as deformation accumulated. One factor that contributes to the development of texture is the martensite morphological change from a lathe to a blocky nature. These twinning (homogenous) and phase change (inhomogeneous) deformation mechanisms achieve the same result of crystallographic reorientation, which concludes that whether the testing format is creep, quasistatic, high strain-rate, compression or tension, both homogenous and inhomogeneous deformation mechanisms can enable crystallographic rotation and need to be considered on a case-by-case basis.

In this work, the straight bar microlattice represents the sample condition with primarily constrained deformation. While the honeycomb microlattice contains both unconstrained and constrained deformation. Lastly, the BCC microlattice operates mainly via unconstrained deformation, with substantial bending around the nodes until fracture. From the previous literature, it is essential to characterize and understand the homogenous and inhomogeneous deformation as both mechanisms play an important role in crystallographic rotation. To better understand the inhomogeneous deformation, pole figure analysis was utilized in tandem with the IPFs to better understand the crystallographic reorientation of honeycomb microlattices in three planes: the orthogonal plane (OP), tensile plane (TP) and build plane (BP, same orientation as IPFs). All directions had a similar (100) texture in both the undeformed gripper and thin-walled sections.

Within the honeycomb struts that bend and eventually align with the TD, a distribution of tensile and compressive forces drives their deformation. It is apparent from the pole figures in Fig. 7(j–l) that the bending deformation (up to 4 % strain) leads to severe out-of-plane texture, eliminating that previously dominant $\langle 100 \rangle$ texture. It is interesting to note that this reorientation primarily occurs in the OD and BD, suggesting the tensile axis acts as an axis of rotation. Near the fracture strain, further out-of-plane rotations were observed in all planes likely due to the initial out-of-

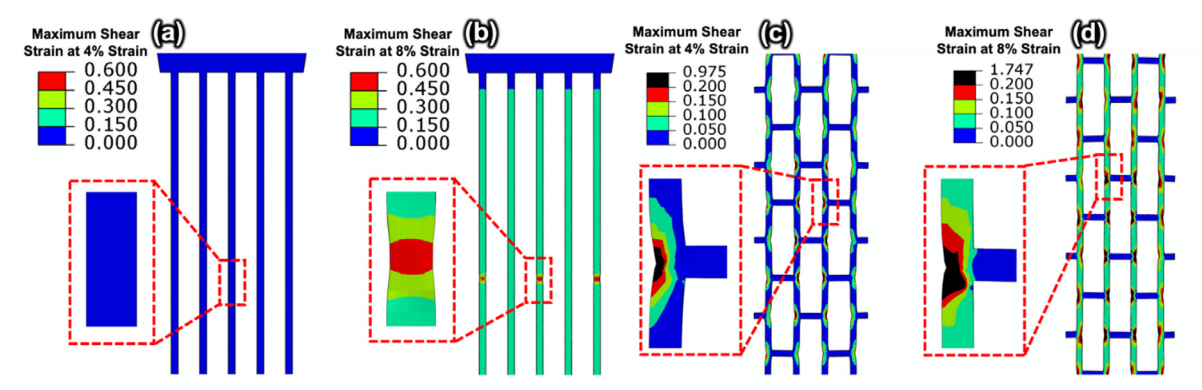


Fig. 8. (a, b) FEM simulation snapshots of the straight bar microlattice at 4 % and 8 % strain. (c, d) FEM simulations of honeycomb microlattice at 4 % and 8 % strain, revealing initial shear strain accumulation near the nodes during the bending phase and continuous shear strain development throughout the honeycomb microlattice up to 8 %, with the nodes maintaining significant levels of shear strain.

plane rotation in the OD and BD. Along the TD two of the four poles rotate out-of-plane likely due to further rotation until the deformation becomes fully stretching-dominated. The degree and exact efficacy of crystallographic rotation are likely varied based on local positional changes of the struts as they align. The other key difference between Fig. 7(g-l and m-o) is that the diffusivity of the poles increases, likely due to the initial elimination of a crystallographic texture and then further propagation with the last stretching step until failure. Due to uneven surfaces after geometrical shrinkage from necking in the BCC microlattices, XRD was utilized to validate and quantify the change in crystallographic texture, rather than EBSD, as seen in Fig. S3. After deformation there is a substantial change from the $\langle 100 \rangle$ texture to a $\langle 111 \rangle$ dominant texture, supporting that these unconstrained deformation mechanisms, in a 2D or 3D design, lead to crystallographic rotation.

KAM mapping has been found to be a confident tool to estimate dislocation density, specifically GND density, as GNDs develop during homogeneous deformation [55,56]. KAM maps in Fig. 6 clearly show dislocation activity and build-up as the deformation increases from 4 % and 8 % strain. From comparing Figs. 5(d) and 6(e, g), we found that the grain morphology in honeycomb microlattices also changes from the AP state to 4 % and the final 8 % strain, starting with a relatively equiaxed microstructure, then it becomes elongated and distorted and finally fragmented, reducing the average grain size. While no deformation twinning was detected, this dislocation activity and the apparent grain fragmentation were observed in the previously mentioned research works on bulk Ni alloys and led to crystallographic reorientation [49,54].

Lastly, Fig. 8 showcases the spatial distribution and accumulation of shear strain along the straightbar and honeycomb microlattices, which has been heavily discussed in the rolling, extrusion and various other communities [57-62]. These sources demonstrate both experimentally and through modeling that an applied rolling or simple compressive force can generate an evolving gradient shear strain that causes crystallographic rotation. Liu et al. [58] showcased how shear strains developed in a rolled Al single crystal coupled with the development of a Goss texture and how the location dependency of crystal texture related to the shear components. Interestingly, the authors, back in 2000, mentioned the need for advanced simulation capabilities to properly model this phenomenon, which is now achievable and again demonstrated in Fig. 8. Inhomogeneous deformation can also lead to grain rotation. Using in-situ tension under high-energy XRD, Li et al. [63], captured clear evidence of crystal rotation near surfaces by 27° in Ti processed by laser shock peening. They ascribe the prominent crystal rotation to inhomogeneous shear deformation as evidenced by the formation of shear bands near surfaces. In the current honeycomb microlattice, the bending and presumably shear have been largely contributing to the initial plastic deformation. As shown in FEM in Fig. 8(c, d), significant shear deformation has indeed been captured near the nodes and lesser amounts throughout the whole sample. Such a large shear strain is likely to introduce substantial crystallographic reorientation. Configurational changes shall be considered as well, with the BCC and honeycomb strut angle changing a total of 32° and 33°, respectively. These inplane changes should cause limited grain rotation. Further conclusions can be made from the predominantly (101) and (111) oriented grains in the IPFs of honeycombs subjected to a strain of 4 % and 8 %. The angles between the (100)-(101) and (100)-(111) planes being 45° and 54.74°, demonstrates that in either 4 % or 8 % strained state, the crystallographic reorientation cannot be fully explained by configurational changes.

The straight bar simulations in Fig. 8(a, b), showcase that there is no shear stress development until near fracture. The lower degrees of shear strain explain the maintained (100) crystallographic texture within the 4 % deformed straight bar microlattice. Other FEM simulations by Jahedi et al. have shed light on how dynamic evolution of both a uniaxial force in combination with a shear force leads to a significantly higher degree of crystal rotation in a simulated polycrystalline sample than simply applying a shear force [61]. This study helps address the continuous shear strain evolution after the bending deformation sequence has been completed (> 4 % strain). This observation is essential to understand and validate the development of shear strain within the simulated microlattice nodes as it continues to grow even after the bending deformation mechanism switches to the stretching mechanism. This deformation-induced grain reorientation is a complex mixture of both homogenous (dislocation activity) and inhomogeneous (shear strain) within the nodes.

Additionally, the honeycomb and BCC microlattices contained struts that were on average 7.5 %–13 % thinner than the straight bar, and still maintained an average ductility 2.5 %–15 % higher, alluding to this microstructural change to explain the prominent ductility enhancement. The variable influence of deformation on differing internal microstructure and crystal orientations of specimens suggests that the intrinsic microstructure as well as extrinsic geometry should be both taken into account when designing future microlattices with advanced performance.

5. Conclusion

This work compares the mechanical behavior among three microlattice designs, a straight bar (acting as a form of reference), an elongated honeycomb and a BCC microlattice. FEM analyses largely captured the *in-situ* measurement of mechanical response

of these microlattices and elucidated the effects of architecture design on the mechanical response of the materials. It is also one of the first studies to show the capability to additively manufacture ODS materials into thin-wall microlattices. The concepts of constrained and unconstrained deformation are important in understanding how the designs that utilize a bending deformation, such as the BCC microlattice, can accommodate large strains and moderate stresses. The two deformation mechanisms, stretching and bending, observed in these microlattice experiments have different influences on crystallographic reorientation, and ultimately necessitate the use of homogenous and inhomogeneous deformation to understand the observed deformation-induced crystallographic rotation. Stretching causes minimal change in the out-ofplane crystallographic orientation but the bending shows the onset of change from a (100) crystallographic orientation to a more randomly oriented crystallographic distribution. This rotation is enabled by the combination of dislocation activity and accumulation of shear strain through plastic deformation, which was confirmed by both EBSD experiments and FEM simulations. This study is one of the first works that reveals severe crystallographic reorientation and grain refinement in honeycomb microlattice during tensile deformation.

Declaration of interests

The authors declare that they have no known competing financial interests or personal relationships that could have appeared to influence the work reported in this paper.

Acknowledgements

Benjamin Stegman and Xinghang Zhang would like to acknowledge the financial support from the NSF-DFG CMMI grant (No. 2228266). Benjamin Stegman and Haiyan Wang acknowledge the partial support from the U.S. Office of Naval Research (ONR, No. N00014-22-1-2160) for microscopy analysis. We also acknowledge access to the microscopy center in the School of Materials Engineering at Purdue University.

Supplementary materials

Supplementary material associated with this article can be found, in the online version, at doi:10.1016/j.jmst.2023.12.070.

References

- [1] C. Zhao, K. Fezzaa, R.W. Cunningham, H. Wen, F. De Carlo, L. Chen, A.D. Rollett, T. Sun. Sci. Rep. 7 (2017) 3602.
- [2] D.K. Koli, G. Agnihotri, R. Purohit, Mater. Today Proc. 2 (2015) 3032-3041.
- [3] M. Pervaiz, S. Panthapulakkal, M. Sain, J. Tjong, Mater. Sci. Appl. 7 (2016) 26-38.
- [4] S. Gangireddy, M. Komarasamy, E.J. Faierson, R.S. Mishra, Mater. Sci. Eng. A 745 (2019) 231-239.
- [5] D. Mahmoud, M.A. Elbestawi, J. Manuf. Mater. Process. 1 (2) (2017) 13.
- [6] D. Chen, X. Zheng, Sci. Rep. 8 (2018) 9139.
- [7] Y. Xue, X. Wang, W. Wang, X. Zhong, F. Han, Mater. Sci. Eng. A 722 (2018) 255-262
- [8] D. Zhang, C. Kenel, D.C. Dunand, Acta Mater. 221 (2021) 117420.
 [9] X.Y. Yap, I. Seetoh, W.L. Goh, P. Ye, Y. Zhao, Z. Du, C.Q. Lai, C.L. Gan, Int. J. Mech.
- Sci. 196 (2021) 106285.
- [10] M.S. Saleh, C. Hu, J. Brenneman, A.M. Al Mutairi, R. Panat, Addit. Manuf. 39 (2021) 101856
- [11] S.H. Kim, S.M. Yeon, J.H. Lee, Y.W. Kim, H. Lee, J. Park, N.K. Lee, J.P. Choi, C. Aranas, Y.J. Lee, S. An, K. Choi, Y. Son, Virtual Phys. Prototyp. 15 (2020) 460-480
- [12] L. Bai, Y. Xu, X. Chen, L. Xin, J. Zhang, K. Li, Y. Sun, Mater. Des. 211 (2021) 110140

- [13] J.K. Algardh, T. Horn, H. West, R. Aman, A. Snis, H. Engqvist, J. Lausmaa, O. Harrysson, Addit, Manuf. 12 (2016) 45-50.
- [14] X. Wang, J.A. Muñiz-Lerma, M. Attarian Shandiz, O. Sanchez-Mata, M. Brochu, Mater. Sci. Eng. A 766 (2019) 138395.
- [15] J. Kangazian, M. Shamanian, A. Kermanpur, F. Sadeghi, E. Foroozmehr, Mater. Sci. Eng. A 853 (2022) 143797.
- [16] H. Irrinki, S.D. Nath, A.A. Akilan, S.V. Atre, J. Alloy. Compd. 901 (2022) 209-219.
- [17] R.E. Schafrik, D.D. Ward, J.R. Groh, Superalloys 718 (2001) 1-11.
- [18] B. Stegman, B. Yang, Z. Shang, J. Ding, T. Sun, J. Lopze, W. Jarosinski, H. Wang, X. Zhang, J. Alloy. Compd. 920 (2022) 165846.
- [19] A. Certain, S. Kuchibhatla, V. Shutthanandan, D.T. Hoelzer, T.R. Allen, J. Nucl. Mater. 434 (2013) 311-321.
- [20] S. Ukai, S. Kato, T. Furukawa, S. Ohtsuka, Mater. Sci. Eng. A 794 (2020) 139863.
- [21] L. Tan, G. Wang, Y. Guo, Q. Fang, Z. Liu, X. Xiao, W. He, Z. Qin, Y. Zhang, F. Liu, L. Huang, Virtual Phys. Prototyp. 15 (2020) 555–569.
- [22] R.L. Klueh, J.P. Shingledecker, R.W. Swindeman, D.T. Hoelzer, J. Nucl. Mater. 341 (2005) 103-114.
- [23] J.R. Groza, J.C. Gibeling, Mater. Sci. Eng. A 171 (1993) 115–125.
- [24] H. Figiel, O. Zogał, V. Yartys, J. Alloy. Compd. 1 (2021) 404-406.
- [25] J. Weidmann, A. Großmann, C. Mittelstedt, Int. J. Mech. Sci. 180 (2020) 105639.
- [26] V. Tvergaard, A. Needleman, Acta Metall. 32 (1984) 157–169.
- [27] P. Li, Mater. Sci. Eng. A 622 (2015) 114-120.
- [28] X. Liu, K. Sekizawa, A. Suzuki, N. Takata, M. Kobashi, T. Yamada, Materials 13 (2020) 2902.
- [29] K. Hazeli, D. June, P. Anantwar, B.B. Babamiri, Addit. Manuf. 56 (2022) 102928.
- [30] A. Namdeo, V. Bhandare, B.J. Sahariah, P. Khanikar, Mater. Sci. Eng. A 855 (2022) 143878.
- [31] U.A. Dar, H.H. Mian, A. Qadeer, M. Abid, R.A. Pasha, M. Bilal, M.Z. Sheikh, in: in: Proceedings of 17th International Bhurban Conference on Applied Sciences and Technology, Islamabad, Pakistan, 2020.
- [32] D. Kuhlmann-Wilsdorf, Mater. Sci. Eng. 39 (1979) 231-245.
- [33] L. Delcuse, S. Bahi, U. Gunputh, A. Rusinek, P. Wood, M.H. Miguelez, Addit. Manuf. 36 (2020) 101339.
- [34] A. Banerjee, S. Messina, M.R. Begley, E.J. Schwalbach, M.A. Groeber, W.D. Musinski, P.A. Shade, M.E. Cox, J.D. Miller, K.J. Hemker, Scr. Mater. 205 (2021) 114188.
- [35] K. Nelson, C.N. Kelly, K. Gall, Mater. Sci. Eng. B 286 (2022) 116013.
- [36] J. Zhang, J. Yanagimoto, Compos. Pt. B-Eng. 224 (2021) 109241
- [37] J. Zhang, Y. Sato, J. Yanagimoto, CIRP Ann-Manuf. Technol. 70 (2021) 111-114.
- [38] J. Zhang, J. Yanagimoto, Compos. Struct. 255 (2021) 112889.
- [39] X.Y. Zhang, G. Fang, S. Leeflang, A.A. Zadpoor, J. Zhou, Acta Biomater. 84 (2019) 437-452
- [40] P. Hanzl, I. Zetková, M. Daňa, Manuf. Technol. 19 (2019) 228-231.
- [41] R. Pokharel, J. Lind, A.K. Kanjarla, R.A. Lebensohn, S.F. Li, P. Kenesei, R.M. Suter, A.D. Rollett, Ann. Rev. Condens. Matter Phys. 5 (2014) 317-346.
- [42] X. Kong, Y. Yang, Z. Sun, H. Yang, Y. Liu, Y. Ren, L. Cui, C. Chen, S. Hao, Appl. Mater. Today 22 (2021) 100904.
- [43] Z. Shang, T. Sun, J. Ding, N.A. Richter, N.M. Heckman, B.C. White, B.L. Boyce, K. Hattar, H. Wang, X. Zhang, Sci. Adv. 9 (2023) eadd9780.
- [44] R. Lawitzki, S. Hassan, L. Karge, J. Wagner, D. Wang, J. von Kobylinski, C. Krempaszky, M. Hofmann, R. Gilles, G. Schmitz, Acta Mater. 163 (2019) 28-39. [45] D. Raabe, D. Ma, F. Roters, Acta Mater. 55 (2007) 4567-4583.
- [46] D.W. Brown, S.P. Abeln, W.R. Blumenthal, M.A.M. Bourke, M.C. Mataya, C.N. Tomé, Metall. Mater. Trans. A 36 (2005) 929-939.
- [47] L. Jin, J. Dong, J. Sun, A.A. Luo, Int. J. Plast. 72 (2015) 218-232.
- [48] J.F. Xiao, C. Cayron, R.E. Logé, Int. J. Plast. 159 (2022) 103468.
- W.D. Musinski, P.A. Shade, D.C. Pagan, J.V. Bernier, Materialia 16 (2021) 101063.
- [50] C.J. Boehlert, Z. Chen, I. Gutiérrez-Urrutia, J. Llorca, M.T. Pérez-Prado, Acta Mater. 60 (2012) 1889-1904.
- [51] L. Zhang, M. Wu, C. Xu, S. Guo, Z.L. Ning, F.Y. Cao, Y.J. Huang, J.F. Sun, J. Yi, Mater. Sci. Eng. A 827 (2021) 142063.
- [52] O. Dumas, L. Malet, B. Hary, F. Prima, S. Godet, Acta Mater. 205 (2021) 116530.
- [53] J.C. Stinville, K. Gallup, T.M. Pollock, Metall. Mater. Trans. A 46 (2015)
- [54] J. Coakley, R.C. Reed, J.L.W. Warwick, K.M. Rahman, D. Dye, Acta Mater. 60 (2012) 2729-2738.
- [55] J. Meng, X. Chen, J. Jiang, L. Liu, Metals (Basel) 13 (2023) 89.
- [56] S.S. Rui, Q.N. Han, X. Wang, S. Li, X. Ma, Y. Su, Z. Cai, D. Du, H.J. Shi, Mater. Today Commun. 27 (2021) 102445.
- [57] H. Miyamoto, T. Xiao, T. Uenoya, M. Hatano, ISIJ Int. 50 (2010) 1653-1659.
- [58] Q. Liu, J. Wert, N. Hansen, Acta Mater. 48 (2000) 4267-4279.
- [59] H. Park, D. Nyung Lee, Mater. Sci. Forum 408-412 (2002) 637-642.
- [60] C. Zhu, T. Harrington, V. Livescu, G.T. Gray, K.S. Vecchio, Acta Mater. 118 (2016) 383-394.
- [61] M. Jahedi, M. Ardeljan, I.J. Beyerlein, M.H. Paydar, M. Knezevic, J. Appl. Phys. 117 (2015) 214309.
- [62] M. Efe, B. Gwalani, J. Tao, M. Song, T.C. Kaspar, A. Devaraj, A. Rohatgi, Appl. Surf. Sci. 562 (2021) 150132.
- [63] R. Li, Y. Wang, N. Xu, Z. Yan, S. Li, M. Zhang, J. Almer, Y. Ren, Y.D. Wang, Acta Mater. 229 (2022) 117810.